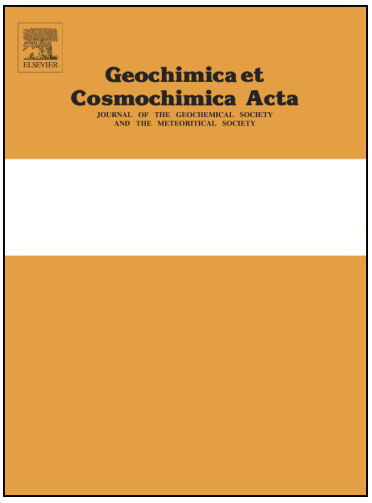

The neutron capture process in the He shell in core-collapse supernovae: Presolar silicon carbide grains as a diagnostic tool for nuclear astrophysics

Marco Pignatari, Peter Hoppe, Reto Trappitsch, Chris Fryer, F.X. Timmes, Falk Herwig, Raphael Hirschi

PII: S0016-7037(17)30353-8
DOI: http://dx.doi.org/10.1016/j.gca.2017.06.005
Reference: GCA 10317

To appear in: *Geochimica et Cosmochimica Acta*

Received Date: 24 October 2016
Revised Date: 1 June 2017
Accepted Date: 1 June 2017

Please cite this article as: Pignatari, M., Hoppe, P., Trappitsch, R., Fryer, C., Timmes, F.X., Herwig, F., Hirschi, R., The neutron capture process in the He shell in core-collapse supernovae: Presolar silicon carbide grains as a diagnostic tool for nuclear astrophysics, *Geochimica et Cosmochimica Acta* (2017), doi: http://dx.doi.org/10.1016/j.gca.2017.06.005

The neutron capture process in the He shell in core-collapse supernovae: Presolar silicon carbide grains as a diagnostic tool for nuclear astrophysics

Marco Pignatari[1,2*], Peter Hoppe[3], Reto Trappitsch[4,2], Chris Fryer[5,2], F.X. Timmes[6,7,2], Falk Herwig[8,7,2] and Raphael Hirschi[9,10,2]

[1]E. A. Milne Centre for Astrophysics, University of Hull, Hull, HU6 7RX, UK

[2]The NuGrid Collaboration (http://www.nugridstars.org)

[3]Max Planck Institute for Chemistry, Hahn-Meitner-Weg 1, 55128 Mainz, Germany

[4]Department of the Geophysical Sciences, The University of Chicago, and Chicago Center for Cosmochemistry, Chicago, IL 60637, USA.

[5]Computational Physics and Methods (CCS-2), LANL, Los Alamos, NM, 87545, USA

[6]Arizona State University (ASU), PO Box 871404, Tempe, AZ, 85287-1404, USA

[7]The Joint Institute for Nuclear Astrophysics, Notre Dame, IN 46556, USA

[8]Department of Physics & Astronomy, University of Victoria, Victoria, BC, V8P5C2 Canada.

[9]Keele University, Keele, Staffordshire ST5 5BG, United Kingdom

[9]Institute for the Physics and Mathematics of the Universe (WPI), University of Tokyo, 5-1-5 Kashiwanoha, Kashiwa 277-8583, Japan

*Corresponding author. E-mail: mpignatari@gmail.com

Submitted to

Geochimica et Cosmochimica Acta

September 28, 2016

Revised May 2, 2017

Abstract.

Carbon-rich presolar grains are found in primitive meteorites, with isotopic measurements to date suggesting a core-collapse supernovae origin site for some of them. This holds for about 1-2 % of presolar silicon carbide (SiC) grains, so-called Type X and C grains, and about 30 % of presolar graphite grains. Presolar SiC grains of Type X show anomalous isotopic signatures for several elements heavier than iron compared to the solar abundances: most notably for strontium, zirconium, molybdenum, ruthenium and barium. We study the nucleosynthesis of zirconium and molybdenum isotopes in the He-shell of three core-collapse supernovae models of 15, 20 and 25 $M_{\odot}$ with solar metallicity, and compare the results to measurements of presolar grains. We find the stellar models show a large scatter of isotopic abundances for zirconium and molybdenum, but the mass averaged abundances are qualitatively similar to the measurements. We find all models show an excess of ^{96}Zr relative to the measurements, but the model abundances are affected by the fractionation between Sr and Zr since a large contribution to ^{90}Zr is due to the radiogenic decay of ^{90}Sr. Some supernova models show excesses of ^{95,97}Mo and depletion of ^{96}Mo relative to solar. The mass averaged distribution from these models shows an excess of ^{100}Mo, but this may be alleviated by very recent neutron-capture cross section measurements. We encourage future explorations to assess the impact of the uncertainties in key neutron-capture reaction rates that lie along the *n*-process path.

1. INTRODUCTION

Core collapse supernova (CCSN) events are the final life stage of massive stars ($M > 8\ M_{\odot}$, e.g., Nomoto et al. 2013, Jones et al. 2013). In CCSN ejecta, several types of dust find favorable conditions to condense. Dust made in old CCSNe before the formation of the solar system can still be identified today in primitive meteorites and their measured isotopic abundances provide crucial information about their parent CCSNe (e.g., Clayton & Nittler 2004, Zinner 2014).

Presolar grains can be distinguished in two large categories categories based on their chemical compositions, O-rich and C-rich grains. C-rich grains most likely require a stellar environment with more C than O to form (C/O > 1). Otherwise, all the C would be bound as CO, and no C-rich molecules and dust could condense efficiently (Ebel & Grossman, 2001). Clayton et al. (1999) and subsequent work explored the possibility to condense C-rich grains from O-rich material, but this scenario is still controversial, also considering the isotopic compositions of presolar C-rich grains (e.g., Lin et al., 2010).

Presolar C-rich grains made by CCSNe are low-density (LD) graphite grains, carrying the Ne-E(L) component (Amari et al. 1990), nano-diamonds carrying the Xe-HL component (Lewis et al. 1987), and silicon carbides (SiC) of Type X (see e.g. Besmehn et al. 2003), of Type C1 (Pignatari et al. 2013) and Type C2 (Liu et al., 2016). At least some of the putative Nova SiC grains were made by CCSNe (Nittler & Hoppe 2005, Pignatari et al. 2015, Liu et al. 2016, Hoppe et al. 2017), and the same may hold for some SiC grains of Type AB (Zinner 2014, Pignatari et al. 2015).

The main diagnostic to infer the origin of presolar grains is the isotopic compositions of light elements (e.g., C, N, O, Si), and the presence of abundance anomalies due to the decay of live radioactive isotopes after grain condensation (e.g., ^{22}Na, ^{26}Al, ^{32}Si, ^{44}Ti, ^{49}V) in single grains. The exception to this are nano-diamonds. Their small size of only a few nanometers makes the analysis of single grains extremely difficult and the majority of the information we have comes from isotopic analyses performed on bulk samples containing billions of nano-diamonds. This may lead to ambiguous results, since only a small fraction or none of the nano-diamonds might be presolar (e.g., Dai et al. 2002, Stroud et al. 2011).

Also available for a subset of single presolar SiC grains from CCSNe are the isotopic abundances of a few elements heavier than Fe. For SiC X grains, isotopic data are available for Ni, Sr, Zr, Mo, Ru and Ba (e.g., Pellin et al. 2006, Marhas et al. 2007, 2008, Kodolányi et al. 2016, Stephan et al. 2017). For a SiC AB grain Mo and Ru isotope data are available, with anomalous signatures that seem to be consistent with a CCSN origin (Savina et al. 2003, 2007). There are no available measurements for heavy elements in SiC Type C1 and C2, or in putative nova grains (e.g., Liu et al. 2016). Nicolussi et al. (1998) measured Zr and Mo in single high-density (HD) graphites, finding two of them with anomalous high ^{96}Zr. While most of presolar HD graphites are considered to condense around low-mass asymptotic giant branch (AGB) stars, some of them may have condensed in CCSN ejecta (Amari et al. 2014), which would be consistent with the ^{96}Zr-excess.

The anomalous Mo isotopic abundances measured in five SiC X grains generated a particular interest. The efficient production of Mo proton-rich stable isotopes ^{92,94}Mo are matter of debate in nuclear astrophysics, where it is not clear what type of p-process in supernovae is responsible of their nucleosynthesis (Rauscher et al. 2013, Pignatari et al. 2016 and references therein). The isotope ^{96}Mo is an s-only isotope, i.e. it is mostly made by the slow-neutron capture process (s-process, e.g., Kaeppeler et al. 2011). In particular, most of the s-process abundance of ^{96}Mo is made in low-mass AGB stars, not in CCSNe (e.g., Bisterzo et al. 2014). Finally, the isotope ^{100}Mo is mostly made by the rapid neutron-capture process (r-process, Thielemann et al. 2011 and references therein).

In SiC X grains, on the other hand, the *p*-process isotopes ^{92,94}Mo, the *s*-process isotope ^{96}Mo, and the *r*-process isotope ^{100}Mo are depleted compared to ^{95}Mo and ^{97}Mo and solar isotope abundances (Pellin et al. 2000, 2006). Such anomalous abundance patterns have been associated with the neutron-burst triggered at the SN shock passage in the He shell of CCSNe (Meyer et al. 2000). Pre-explosive He shell nucleosynthesis in massive stars is characterized by partial He-burning, causing ^{12}C to be more abundant than ^{16}O, and by a mild *s*-process signature due to partial activation of the ^{22}Ne(α,n)^{25}Mg reaction (e.g., Limongi et al. 2000, Rauscher et al. 2002). The condition of C/O > 1 makes the He-burning ejecta a suitable environment for presolar SiC grains to condense, in particular in the C/Si zone formed at the bottom of the He shell (Pignatari et al. 2013). The He shell abundances are modified by the SN shock passage. Material is compressed and temperature and density quickly reach a maximum, followed by an expansion where they subsequently decrease rapidly on a timescale of a second (e.g., Woosley et al. 2002). The high peak temperature causes an efficient activation of the ^{22}Ne(α,n)^{25}Mg reaction, which triggers a neutron burst with neutron density peaks up to 10^{18} neutrons cm^{-3} or higher. This nucleosynthesis process was called the *n*-process. The ^{22}Ne fuel to power the n-process is made from the initial CNO abundances, making this process secondary. After being proposed as a potential scenario to explain the r-process, the *n*-process conditions appeared to be not suitable to produce the r-process abundance pattern observed in the Solar System, and therefore this scenario was ruled out (Blake et al. 1976, Thielemann et al. 1979, Blake et al. 1981). Nevertheless, the isotopic distribution of heavy nuclei is strongly affected by this neutron burst, and Meyer et al. (2000) showed that the *n*-process may be compatible with the ^{95}Mo and ^{97}Mo excess observed in SiC X grains.

Alternative scenarios to explain neutron-capture signatures in Mo and in all other elements measured in SiC X grains include the neutrino-wind components from the forming neutron star as a source (Hallmann et al. 2013, Bliss & Arcones 2014). In this work, we will instead consider the most established scenario to explain the Mo isotopic signature, i.e., where the neutron burst triggered by the ^{22}Ne(α,n)^{25}Mg reaction is the responsible source.

The paper is organized as follows. In Section 2 we describe stellar models and the nucleosynthesis for Zr and Mo isotopes, in Section 3 we define the method to compare theoretical results with measurements for SiC X grains. Finally, in Section 4 results are summarized.

2. Results

2.1. Stellar models

In this study, we consider three SN explosion models for stars with initial masses of 15, 20, and 25 $M_\odot$, and metallicity Z = 0.02 (Pignatari et al., 2016; models 15d, 20d and 25d, respectively). The metallicity is the fraction of material that is not hydrogen or helium. The massive star progenitors are computed with the stellar evolution code GENEC (Eggenberger et al., 2008). The SN explosion simulations are based on the fallback prescription by Fryer et al. (2012). The initial shock velocity used beyond fallback is $2 \cdot 10^9$ cm s^{-1}. The post-processing code MPPNP is used to calculate the nucleosynthesis in the star before and during the explosion, adopting a network of more than 5000 isotopes (see Pignatari et al., 2016, for details). In particular, the network is well suited to cover the complete *n*-process path, involving radioactive isotopes with up to ten more neutrons compared to the stable isotopes belonging to the same element.

2.2. Nucleosynthesis in the explosive He-burning shell: Zr and Mo

As we have mentioned in the Introduction, the n-process is due to the activation of the $^{22}Ne(\alpha,n)^{25}Mg$ reaction in the explosive He-burning shell. Since we are interested in the *n*-process products, we focus on the C-rich explosive He burning layers, including the He/C zone, the C/Si zone and a small part of the O/C zone (Meyer et al. 1995, Pignatari et al. 2013). The conditions for the activation of the $^{22}Ne(\alpha,n)^{25}Mg$ reaction change depending on the considered He shell zone: the neutron density peak reaches values exceeding 10^{20} neutrons cm^{-3} in the C/Si zone, while lower densities are obtained in the He/C zone and outward. During the SN shock the temperature at the bottom of the He-shell where the C/Si zone eventually forms changes by about a factor of three between model 15d and model 25d ($2.3 \cdot 10^9$ K and $0.7 \cdot 10^9$ K, respectively, Pignatari et al. 2013). The electron fraction (Y_e) is being mostly set by the ^{22}Ne abundance in models 15d and 20d (Y_e = 0.4993 and 0.4986 in the He shell, respectively), which in turn depends on the metallicity of the progenitor. The amount of ^{22}Ne depleted by nuclear reactions during the SN shock at the bottom of the He shell depends mostly on the SN explosion energy, while it is negligible in the outer part of the He shell. The model 25d instead shows a preSN Y_e in the He shell between 0.5052 and 0.5205, due to the ingestion of hydrogen before the progenitor exploding as a supernova (Pignatari et al. 2015).

In the present study, we explore the production of Zr (Z=40) and Mo (Z=42). The abundances as a function of mass coordinate of the key species ^4He, ^{12}C, ^{16}O, and ^{28}Si are shown in Fig. 1 together with the stable Zr isotopes $^{90,91,92,94,96}Zr$ for model 15d. The key species can be used to identify the relevant CCSN nucleosynthesis in this part of the ejecta. Zones 2 ($M=3.15M_\odot$), 3 ($M=3.50M_\odot$) and 4 ($M=3.85M_\odot$) in the figure are representative of the He/C zone. They

include about 0.01$M_\odot$ each. Zone 1 (M=2.95$M_\odot$) has a similar size, and is representative of the C/Si zone. As shown in Fig. 1, at the bottom of the He/C zone ^{16}O is destroyed, feeding the production of heavier species like ^{28}Si via α-captures. In contrast, ^{12}C is not efficiently depleted, due to the much lower α-capture rate compared to the ^{16}O(α,γ)^{20}Ne reaction. In these conditions, the C/Si zone is formed at the bottom of the He/C zone by the SN shock, where C and Si are the most abundant elements (Pignatari et al. 2013).

In Fig. 1 the abundance profiles of Zr isotopes show large variations within the C-rich stellar layers (M>2.92$M_\odot$ in the figure). In zone 1 (representative of the C/Si zone) there are large abundance variations, with ^{96}Zr typically less abundant than the lighter Zr isotopes. In zone 2, ^{90}Zr is the most abundant isotope, but with more significant enrichments for other Zr isotopes compared to the initial composition. In zone 3, ^{96}Zr is the most abundant isotope, and finally in zone 4 ^{90}Zr is again the most abundant Zr isotope. Zone 4 and the most external He shell layers are not modified by the SN shock. They carry a mild *s*-process nucleosynthesis signature with a small ^{96}Zr deficit, due to the partial activation of the ^{22}Ne(α,n)^{25}Mg reaction. For model 15d, the Zr isotope composition in these more external He-shell layers is not far from the solar abundance distribution. The main goal in showing these profiles, is to make clear that they are indeed complicated. There is not a particular *n*-process signature, given from some specific neutron density. Meyer et al. (2000) discussed the *n*-process nucleosynthesis for a single setup of initial abundances (weak s-process seeds), temperature and density peak (temperature = 10^9 K and density = 1500 g cm^{-3}, respectively). Instead, in model 15d as well as the other models presented in this work the He shell is made out of hundreds of mass zones. Since the pre-SN He shell is convective, the composition of most of these zones at the onset of the SN explosion is relatively homogeneous. However, the SN shock conditions significantly change across the C-rich zones shown in Fig. 1, depending on their distance from the center of the star (e.g., Woosley et al. 2002). The temperature (density) peaks calculated for model 15d are $2.0\cdot10^9$ K ($7.5\cdot10^3$ cm^{-3}), $1.3\cdot10^9$ K ($2.1\cdot10^3$ cm^{-3}), $0.9\cdot10^9$ K ($6.2\cdot10^2$ cm^{-3}) and $0.7\cdot10^9$ K ($2.3\cdot10^2$ cm^{-3}) in zones 1, 2, 3 and 4, respectively. Consequently, the neutron density varies by orders of magnitude, up to values beyond 10^{20} neutrons cm^{-3} in the C/Si zone.

Under these conditions the heavy isotopes may have different production channels in different He-shell zones. In Fig. 2, we show in detail the production of ^{90}Zr. It is only in zone 4 that ^{90}Zr does not receive a substantial contribution from its radioactive, neutron-rich isobars. At 2.5 seconds after the SN shock in zone 3, ^{90}Sr is the most abundant species among the radioactive parents of ^{90}Zr. In zone 1 and 2, ^{90}Kr is instead the most abundant isobar.

Similar large variations are observed for Mo isotopes (Fig. 3). As for Zr, in zone 1 there are large variations, but overall ^{95}Mo and the r-only ^{100}Mo are the most abundant Mo isotopes. In zone 2, ^{95}Mo is the most abundant Mo isotope, the same holds for ^{97}Mo in zone 3. Finally, zone 4 shows close to initial abundances. Not shown in the figure, the p-process isotopes ^{92,94}Mo are depleted in zones 1, 2 and 3, and only reduced by a small amount in zone 4. ^{100}Mo shows a complex profile. From Fig. 4, the abundant ^{100}Mo peak between zones 3 and 4 is due to direct production of ^{100}Mo, which is formed via neutron capture from lighter Mo species. In the rest of the He-shell layers ^{100}Mo originates from the decay of radioactive ^{100}Zr, formed in a neutron-capture path far from the valley of stability.

In Fig. 3, the depletion of the *s*-process isotope ^{96}Mo can be clearly seen. Therefore, the deficiency of ^{96}Mo compared to the nearby species ^{95}Mo and ^{97}Mo, all measured in SiC X grains (Pellin et al. 2006, Zinner 2014), does not come as a surprise. All of the other Mo species shown in Fig. 3 are instead enhanced in extended He shell regions. As for ^{100}Mo, the final complex profile of ^{95,97,98}Mo is due to the contribution from different nucleosynthesis paths in the He shell. This makes the analysis of the *n*-process abundance patterns a powerful diagnostic for nuclear astrophysics. The neutron capture rates far from the valley of stability can only be provided by theory at the moment, and the impact of their uncertainties needs to be taken into account during the direct comparison with observations.

The model 20d show similar n-process nucleosynthesis compared to model 15d, and we will see in the next sections that similar isotopic ratios for Zr and Mo are also obtained. On the other hand, in the model 25d the SN shock produces much smaller temperature and density peaks compared to the models 15d and 20d, resulting in much milder isotopic anomalies with respect to the initial composition in the final ejecta.

3. Discussion

We have presented the abundance patterns of Zr and Mo for model 15d. We showed that there is not only one *n*-process pattern in the explosive He shell. Instead, the large range of SN conditions that are naturally found in the explosive He-burning layers of the ejecta generate a large variety of isotopic patterns. A relevant point to clarify before moving forward is how Zr and Mo made their way into presolar grains. Previous works have found a complex sub-grain zoo in stellar dust (Zinner 2014 and references therein). Are there sub-grains dominating the whole grain signature observed for heavy elements in X grains? The answer is probably no.

Low-density graphite grains, believed to have formed in SN explosions, contain abundant TiC subgrains, but no subgrains rich in heavy elements such as Mo are observed in high-density graphite grains, believed to come from AGB stars (see e.g., Croat et al., 2003). In SiC X grains there are Fe-and Ni-rich subgrains (Marhas et al., 2008; Hynes et al., 2010), and Ti-rich subgrains have been identified, e.g., in the Bonanza grain (e.g., Zinner et al., 2011, Gyngard et al. 2017, submitted to the same GCA issue). In contrast, no evidence for subgrains rich in heavy elements in X grains was found. Therefore, for now we will assume that heavy elements like Zr and Mo are uniformly distributed in SiC X grains, and have no subgrain carriers.

3.1. Zr: Model predictions vs. SiC X grain data

In Fig. 5a, we show the Zr production factors normalized to ^{94}Zr for models 15d, 20d, and 25d, integrated over hundreds of zones in the C-rich He shell layers weighted by mass. This simple approach is assuming complete mixing of all the C-rich zones. However, typically heterogeneous mixtures of stellar ejecta are needed to consistently reproduce all isotopic ratios in single grains. More detailed mixing recipes guided by matching also other isotopic ratios can be tested in future works. For model 15d the mass range considered is 2.92-4.51 $M_{\odot}$, and for models 20d and 25d 4.68-6.66 $M_{\odot}$ and 6.82-9.23 $M_{\odot}$, respectively. The zone resolution of stellar models may change significantly across the ejected material.

Assuming a similar SN explosion energy for the three models, the power of the SN shock in the He shell layers becomes weaker with increasing progenitor mass. Therefore, Fig. 5 provides a good indicator of the impact of varying the initial mass of the CCSN progenitor. We would have obtained an analogous effect on the *n*-process products by changing the SN explosion energy for the same massive star progenitor. The isotope ^{96}Zr is enhanced compared to the other Zr species in all cases. For comparison, in the same figure we show the abundance patterns observed for two SiC X grains B2-05 and 196-5 by Pellin et al. 2006, which have the highest (lowest) ^{96}Zr/^{94}Zr ratio and the lowest (highest) ^{90}Zr/^{94}Zr ratio, respectively, among the studied SiC X grains. The range of ^{96}Zr-excess obtained is consistent with the observed range. This result is remarkable, considering that we are averaging over hundreds of zones with different abundance patterns. Interestingly, model 20d shows a higher ^{96}Zr/^{94}Zr ratio than model 15d, where the He shell is exposed to more extreme conditions. There is no linear relation between the ^{96}Zr/^{94}Zr ratio and the progenitor mass (or the SN explosion energy). This nonlinearity is due to the fact that most of the Zr species are made both directly and as radiogenic products. In models 15d and 20d, ^{94}Zr receives a major contribution from the radiogenic decay of ^{94}Sr. Depending on the material ejected ^{96}Zr is made as ^{96}Sr, ^{96}Y or directly as ^{96}Zr in model 15d, and as ^{96}Y and ^{96}Zr in model 20d. In contrast, in model 25d the n-process is significantly weaker compared to the models with smaller initial mass, and the radiogenic contribution is not relevant for ^{96}Zr.

In Fig. 5a the ^{90}Zr-depletion compared to solar measured in grain B2-05 is not reproduced. However, for Zr there is another caveat to keep in mind when stellar nucleosynthesis calculations are compared with measurements in presolar grains. In Fig. 2, we showed that most of the radiogenic ^{90}Zr is made as ^{90}Kr and its daughter species ^{90}Sr. ^{90}Kr has a half-life of only 32 s and will be fully decayed when dust forms in the SN ejecta. However, ^{90}Sr has a half-life of 28.64 years. Since stellar dust condenses in the SN ejecta in the first months to years after the explosion, this means that ^{90}Zr and ^{90}Sr (including the decayed ^{90}Kr) condense as two separated species in SiC X grains, according to the thermodynamic properties of Zr and Sr, respectively. As far as the condensation into SiC is concerned, Zr, Nb, and Mo are expected to condense well into SiC, in contrast to Sr. This is evidenced by high abundances of Zr and Nb in SiC grains and the fact that Sr is depleted relative to Zr and Nb (Amari et al. 1995). These observations are in line with theoretical calculations of SiC condensation by Lodders & Fegley (1997):

Zr, Nb, and Mo condense completely into SiC but Sr does not. In Fig. 5b we show again the Zr abundance patterns as in Fig. 5a, but assuming an arbitrary Zr/Sr fractionation of a factor of 10 during grain formation. As expected only ^{90}Zr is affected with respect to Fig. 5a, obtaining a lower ^{90}Zr/^{94}Zr ratio.

As mentioned earlier, the average used for Fig. 5 is based on the assumption of complete mixing of the C-rich ejecta. This is too simple to reproduce all measured isotopic ratios. For instance, the solar-normalized ^{12}C/^{13}C, ^{29}Si/^{28}Si and ^{30}Si/^{28}Si ratios for the mixture considered in Fig. 5 are 1449, 3.09 and 4.02 (15d), 16234, 2.81 and 4.34 (20d) and 0.31, 5.81 and 3.04 (25d). Both B2-05 and 196-5 are ^{28}Si-rich compared to solar, while the considered average is ^{28}Si-poor.

In Fig. 6, we report the same results as in Fig. 5, but for an average weighted by mass and "efficient" ^{12}C available for condensation of C-rich dust (i.e., with $\Delta(^{12}C) = X(^{12}C)-X(^{16}O)$, Fig. 6a) and weighted by mass, "efficient" ^{12}C and Si abundance (Fig. 6b). The same C-rich ejecta are used as in Fig. 5. The relative ^{12}C/^{13}C, ^{29}Si/^{28}Si and ^{30}Si/^{28}Si ratios are reported in the Figure caption. The average in Fig. 6a is characterized by a stronger weight of the C/Si zone and the deeper He/C zone compared to the most external parts of the He/C zone, while that in Fig. 6b is more affected by the C/Si zone ejecta. In both cases, we do not consider possible Sr/Zr fractionation. The only mixture with ^{28}Si-excess is obtained in Fig. 6b for model 15d, but with a strong ^{12}C-excess. In this scenario we obtain a ^{96}Zr/^{94}Zr ratio higher than solar, but ^{91,92}Zr/^{94}Zr ratios about a factor of two lower than solar. Finally, a ^{90}Zr/^{94}Zr ratio lower than solar is obtained, also without considering Sr/Zr fractionation.

As mentioned at the beginning of this section, heavy elements in SiC X grains are likely condensing together with C and Si. This means that Zr and Mo together with the other heavy elements (when available) should be used to test mixture recipes together with light isotopes. Interestingly, the different types of average tested in this section all yield in general ^{96}Zr-excesses, and, considering the uncertainty on the Sr/Zr fractionation, also the observed scatter for the ^{90}Zr/^{94}Zr ratio is a robust result. In contrast, the isotopic ratios of C and Si are strongly affected by the type of mixture. Thanks to the strong signature of the C/Si zone, model 15d seems to be better suited to produce SiC X grains that are ^{28}Si-rich (see Pignatari et al. 2013) and showing n-process abundance patterns, compared to models 20d and 25d. Excepting model 25d, all of the mixtures show ^{12}C/^{13}C ratios higher than solar. The subsolar C ratio in model 25d is due to the ingestion of H in the He shell just before the CCSN event, producing large quantities of ^{13}C (Pignatari et al. 2015). The production of heavy elements will also need to be explored in detail in CCSN H-ingestion models.

3.2. Mo: Model predictions vs. SiC X grain data

In Fig. 7, the Mo production factors averaged in the same way as Figure 5 and normalized to ^{98}Mo are shown. For comparison, in the same figure we report the abundance pattern observed for two SiC-X grains B2-05 and 113-3 by Pellin et al. (2006). The Mo abundance pattern measured in B2-05 and 113-3 are representative of the n-process signature observed in SiC X grains, where B2-05 is the grain showing the largest anomalies in ^{95}Mo and ^{97}Mo with respect to ^{98}Mo. Models 15d and 20d show an excess in ^{95}Mo and ^{97}Mo, but also a smaller enhancement in ^{100}Mo, which is not observed in the SiC X grains. Model 25d shows milder signatures, as expected. In this model there is no ^{100}Mo enhancement, ^{97}Mo is enhanced but ^{94}Mo is higher than ^{95}Mo, which is not observed. However, this hint alone on Mo would not rule out model 25d from the analysis. Indeed, there are several C-rich layers ejected in the He/C zone with ^{95}Mo- and ^{97}Mo-enrichments. The ^{95}Mo/^{98}Mo and ^{97}Mo/^{98}Mo ratios could be enhanced within mixing recipes with more material from those layers.

Another anomaly not well reproduced by the models is the relative pattern of ^{92}Mo/^{98}Mo with respect to ^{94}Mo/^{98}Mo. The ratios are both sub-solar, as it would be expected in a stellar environment with neutron-capture processes activated and depleting the p-process isotopes. However, stellar models tend to predict a stronger depletion of ^{92}Mo compared to ^{94}Mo, while presolar grains do not show this signature.

Despite the ^{100}Mo enhancement in the 15d and 20d models and the ^{92}Mo/^{94}Mo trend, we also find the results for Mo promising. Not shown in the figure, the ^{95}Mo- and ^{97}Mo-excesses are obtained also with other types of mixtures (see the discussion in Fig. 6 for Zr, and data in Tables 2 and 3), and it is a robust result of the n-process as indicated before by Meyer et al. (2000), despite the large variations of Mo isotopic production within the C-rich ejecta (Figure 3). The predicted ^{100}Mo-excess needs to be evaluated taking into account nuclear uncertainties. In Fig. 8, the integrated abundance pattern for model 15d is compared with the isotopic patterns in zones 1, 2, 3, and 4 (see Fig. 3). Zone 4 shows a mild *s*-process pattern with small enhancements in ^{94}Mo and ^{96}Mo, and depletions in ^{92}Mo and ^{100}Mo. Zone 3 shows a ^{100}Mo/^{98}Mo ratio lower than solar, and excesses in ^{95}Mo and ^{97}Mo. Zones 1 and 2 show a ^{100}Mo/^{98}Mo ratio higher than solar. In these mass regions, the final abundance of ^{100}Mo depends on the production of ^{100}Zr. This is a typical case where nuclear astrophysics needs to be taken into account. For the nucleosynthesis calculations of models 15d, 20d, and 25d, we have used the latest experimental cross sections of the stable Zr isotopes (Tagliente et al. 2012). However, Lugaro et al. (2014) provided a new evaluation of the ^{95}Zr(n,γ)^{96}Zr cross section based on the measurements on neighbor Zr species, which is more than a factor of two lower compared to the older rates used in this work (e.g., Bao et al. 2000). This would increase the production of ^{95}Zr by about a factor of two, increasing its radiogenic contribution to ^{95}Mo, at the expenses of heavier Zr species along the *n*-process path. The impact on the production of ^{97,98,100}Mo of the neutron-capture cross sections of Zr isotopes ^{95,97}Zr needs to be evaluated with a specific study. The results of Lugaro et al. (2014) seem to go in the right direction, boosting (at least) ^{95}Mo compared to ^{100}Mo. Note also that a lower ^{95}Zr(n,γ)^{96}Zr cross section would not remove the ^{96}Zr-excess obtained with the n-process, since in most of the models an important fraction of ^{96}Zr is made from the radiogenic decay of the neutron-rich radioactive isotopes ^{96}Sr and ^{96}Y (see previous section).

Theoretical results shown in Fig. 5 and 7 are summarized in Table 1. The results shown in Fig. 6 for Zr and the analogous data for Mo are given in Table 2 and Table 3, respectively. In the tables we also report the $^{12}C/^{13}C$, $^{29}Si/^{28}Si$ and $^{30}Si/^{28}Si$ ratios normalized to solar for the different mixtures discussed in the text.

4. SUMMARY AND CONCLUSIONS

We report here a detailed analysis of Zr and Mo production by the *n*-process in the He shell in CCSNe of massive stars. We considered for the analysis three CCSNe models of the He shell, for different initial progenitor masses M=15, 20 and 25 $M_{\odot}$, and metallicity Z=0.02.

We showed that, for Zr and Mo (but the same conclusions will hold for other elements), the resulting nucleosynthesis and isotopic distributions are strongly changing across the He shell. The pre-SN abundances are modified at the bottom of the He/C zone and in the C/Si zone. On the other hand, the external part of the He shell is not modified by the SN explosion, carrying a mild *s*-process signature due to the $^{22}Ne(\alpha,n)^{25}Mg$ activation before the SN explosion. Therefore, we cannot clearly identify a typical *n*-process pattern in the explosive He shell. The anomalous abundance pattern measured in SiC X grains for Zr, Mo, and other elements is instead given by the composition of many different zones in the C-rich explosive He-burning ejecta.

As a working hypothesis, we integrated the isotopic abundances with a weighted average via the mass of material in the C-rich He shell ejecta. For Zr, the resulting isotopic abundances show a $^{96}Zr/^{94}Zr$ ratio higher than solar for all the models considered. The $^{90}Zr/^{94}Zr$ ratio is affected by the fractionation Zr:Sr, since most of the radiogenic ^{90}Zr is still in the form of ^{90}Sr for the typical timescale of SiC grains condensation. For Mo, the 15 and 20 $M_{\odot}$ models show enhanced $^{95}Mo/^{98}Mo$ and $^{97}Mo/^{98}Mo$ ratios and depleted $^{96}Mo/^{98}Mo$ ratio, as observed in presolar SiC X grains. However, ^{100}Mo is enhanced as well, which is not observed. This is probably due to the uncertainty of the neutron-capture reaction rates of the unstable species in the *n*-process path. In our calculations, the isotope ^{100}Mo is made directly, or as a radiogenic product of ^{100}Zr. A recent revision of the neutron-capture cross section of the unstable isotope ^{95}Zr is going to increase the production of ^{95}Mo compared to other Mo isotopes. The impact on Mo of the nuclear uncertainties of unstable Zr isotopes needs to be taken into account. Finally, the 25d model does not show an excess in ^{100}Mo, but a mild enrichment is obtained also for ^{94}Mo, due to the lower temperatures reached in the He shell in this model compared to lower masses at the SN shock passage.

We tested two additional mixtures of the C-rich ejecta of the He shell, with weighted averages taking into account also the abundance of ^{12}C relative to ^{16}O, and the abundance of Si. Large changes are obtained for isotopic ratios of light elements like C and Si, but overall the main isotopic signatures on Zr and Mo are not so affected.

An important thing to keep in mind is that the models adopted for these calculations are based on one-dimensional stellar progenitors. The final abundances in the He shell layers are sensitive to the peak density and temperature associated to the SN shock, which quantitatively depend on the pre-shock structure. In Pignatari et al. (2015), we have seen that ingestion of H could drastically affect not only the production of light elements, but also strongly reduce the n-process activation. On the other hand, in following works like Liu et al. 2016 it has been shown that neutron capture signatures are observed together with H-ingestion signatures. This is an indication that strong asymmetries are present in the He shell during the CCSN explosion, due to the pre-SN H-ingestion event. This is consistent with multi-dimensional hydrodynamics stellar simulations of these events (Herwig et al. 2014).

Therefore, stellar evolution uncertainties can also have a relevant impact on the *n*-process products. In addition, SN explosion in one-dimensional models are artificial. The multi-dimensional nature of CCSN explosions and the details of SN-shock propagation across different stellar layers are not properly taken into account. The impact of stellar uncertainties can be difficult to disentangle from the impact of nuclear physics uncertainties. However, with the nuclear physics involved under control, the analysis of the abundances in SiC X grains can help to constrain the physics conditions in the He- and C-rich layers of real CCSNe, that made those grains.

With simple averages over the He-shell material, our stellar models are capable of qualitatively reproducing the abundance pattern for Zr and Mo observed in SiC X grains. These promising results need to be confirmed by taking into account the nuclear uncertainties and stellar uncertainties involved along the *n*-process path. The same analysis will be extended to Sr, Ru and Ba in future work.

Acknowledgements. This work is mainly based on the research made in September 2013 in collaboration with Ernst Zinner. The authors deeply thank Ernst for his guidance and contribution, that were crucial in obtaining these results. With Ernst we shared the enthusiasm, the joy for new discoveries and the wonder at the next mystery to be solved. It has been a beautiful journey, and we will continue along this path started with Ernst. We will solve the next mystery, and thanks to Ernst's work there are still many more that are challenging what we know about stars. Thanks for the journey, Ernst.

We thank Yangting Lin, two anonymous referees, and guest editor Larry Nittler for constructive and helpful reviews. NuGrid acknowledges significant support from NSF grants PHY 02-16783 and PHY 08-22648 (Joint Institute for Nuclear Astrophysics, JINA), NSF grant PHY-1430152 (JINA Center for the Evolution of the

Elements) and EU MIRG-CT-2006-046520. The continued work on codes and in disseminating data is made possible through funding from STFC and EU-FP7-ERC-2012-St Grant 306901 (RH, UK), and NSERC Discovery grant (FH, Canada). MP acknowledges support from the "Lendulet-2014" Programme of the Hungarian Academy of Sciences, from SNF (Switzerland) and thanks the resource allocations on the University of Hull High Performance Computing Facility viper. NuGrid data is served by Canfar/CADC. RT is supported by NASA Headquarters under the NASA Earth and Planetary Science Fellowship Program through grant NNX12AL85H and was partially supported by the NASA Cosmochemistry Program through grant NNX09AG39G (to A. M. Davis).

REFERENCES

Amari S., Anders A., Virag A. and Zinner E. (1990) Interstellar graphite in meteorites. *Nature* **345**, 238-240.

Amari S., Hoppe P., Zinner E. and Lewis R.S. (1995) Trace-element concentrations in single circumstellar silicon carbide grains from the Murchison meteorite. *Meteoritics* **30**, 679-693.

Amari S., Zinner E. and Gallino R. (2014) Presolar graphite from the Murchison meteorite: An isotopic study. *Geochim. Cosmochim. Acta* **133**, 479-522.

Bao Z.Y., Beer H., Käppeler F., Voss F., Wisshak K. and Rauscher T. (2000) Neutron cross sections for nucleosynthesis studies. *ADNDT* **76**, 70-154.

Bisterzo, S., Travaglio, C., Gallino, R., Wiescher, M., Käppeler, F. (2014), Galactic Chemical Evolution and Solar s-process Abundances: Dependence on the ^{13}C-pocket Structure, *ApJ* **787**, 10

Blake J.B. and Schramm D.N. (1976) A possible alternative to the r-process. *ApJ* **209**, 846-849.

Blake J.B., Woosley S.E., Weaver T.A. and Schramm D.N (1981) Nucleosynthesis of neutron-rich heavy nuclei during explosive helium burning in massive stars. *ApJ* **248**, 315-320.

Besmehn A. and Hoppe P. (2003) A NanoSIMS study of Si- and Ca-Ti-isotopic compositions of presolar silicon carbide grains from supernovae. *Geochim. Cosmochim. Acta* **67**, 4693-4703.

Bliss J. and Arcones A. (2014) Nucleosynthesis of Mo in neutrino-driven winds. *Nuclei in the Cosmos NIC-XIII,* (p. 111). Hungary: Institute for Nuclear Research of the Hungarian Academy of Sciences.

Clayton D.D., Liu W. and Dalgarno A. (1999) Condensation of carbon in radioactive supernova gas. *Science* **283**, 1290-1292.

Clayton D.D. and Nittler L.R. (2004) Astrophysics with Presolar Stardust. *ARAA* **42**, 39-78.

Croat T.K., Bernatowicz T.J., Amari S., Messenger S. and Stadermann F.J. (2003) Structural, chemical, and isotopic microanalytical investigations of graphite from supernovae. *Geochim. Cosmochim. Acta* **67**, 4705-4725.

Ebel D.S. and Grossman L. (2001) Condensation from supernova gas made of free atoms. *Geochim. Cosmochim. Acta* **65**, 469-477.

Eggenberger P., Meynet G., Maeder A., Hirschi R., Charbonnel C., Talon S. and Ekström S. (2008) The Geneva stellar evolution code. *Ap&SS* **316**, 43-54.

Fryer C.L., Belczynski K., Wiktorowicz G., Dominik M., Kalogera V. and Holz D.E. (2012) Compact remnant mass function: Dependence on the explosion mechanism and metallicity. *The Astrophys. J.* **749**, 91 (14pp).

Gyngard F., Jadhav M., Nittler L.R., Stroud M.R., and Zinner E. (2017) Bonanza: An extremely large dust grain from a supernova, *Geochim. Cosmochim. Acta,* this issue.

Hallmann O., Farouqi K., Kratz K.-L., Ott U. (2013) Origin of anomalous Zr, Mo and Ru abundances in SiC X-grains: Indications of a primary charged-particle process. *Meteorit. Planet. Sci. Supp.* **76**, 5082.

Herwig F., Woodward P.R., Lin P.-H.; Knox M., Fryer C. (2014) Global Non-spherical Oscillations in Three-dimensional 4π Simulations of the H-ingestion Flash, *ApJ Letters,* **792**, 3

Hoppe P., Pignatari M., Kodolányi J., Gröner E., and Amari S. (2017) NanoSIMS isotope studies of rare types of presolar silicon carbide grains from the Murchison meteorite: Implications for supernova models and the role of ^{14}C. *Geochim. Cosmochim. Acta* **this issue.**

Hynes M.K., Croat K.T., Amari S., Mertz A.F. and Bernatowicz T.J. (2010) Structural and isotopic microanalysis of presolar SiC from supernovae. *Meteorit. Planet. Sci.* **45**, 596-614.

Jones S., Hirschi R., Nomoto K., Fischer T., Timmes F. X., Herwig F., Paxton B., Toki H., Suzuki T., Martínez-Pinedo G., Lam Y. H. and Bertolli M. G. (2013) Advanced burning stages and fate of 8-10 M ☉ Stars. *Astrophys. J.* **772**, 150 (14pp).

Lewis R.S., Tang M., Wacker J.F., Anders E. and Steel E. (1987) Interstellar diamonds in meteorites. *Nature* **326**, 160-162.

Käppeler, F., Gallino, R., Bisterzo, S., Aoki, Wako (2011) The s process: Nuclear physics, stellar models, and observations, *Review of Modern Physics*, **83**, Issue 1, 157-194

Kodolányi J., Stephan T., Trappitsch R., Hoppe P., Pignatari M., Davis A.M., and Pellin M.J. (2016) Iron and nickel isotope measurements on SiC X grains with CHILI. *LPI* **1921**, 6443.

Limongi M., Straniero O. and Chieffi A. (2000) Massive stars in the range 13-25 M_{solar}: Evolution and nucleosynthesis. II. The solar metallicity models. *Astrophys. J. Supp. Ser.* **129**, 625-664.

Lin Y., Gyngard F. and Zinner E. (2010) Isotopic analysis of supernova SiC and Si_3N_4 grains from the Qingzhen (EH3) chondrite. *Astrophys. J.* **709**, 1157-1173.

Liu N., Nittler L.R., Alexander C.M.O.D., Wang J., Pignatari M., José J. and Nguyen A. (2016) Stellar origins of extremely ^{13}C- and ^{15}N-enriched presolar SiC grains: Novae or supernovae? *The Astrophysical Journal* **820**, 140 (14pp).

Lodders K. and Fegley, Jr. B. (1997) Complementary trace element abundances in meteoritic SiC grains and carbon star atmospheres. *Astrophys. J. Lett.* **484**, L71-L74.

Lugaro M. Tagliente G., Karakas A.I., Milazzo P.M., Käppeler F. Davis A.M., Savina M.R. (2014) The impact of updated Zr neutron-capture cross sections and new asymptotic giant branch models on our understanding of the s process and the origin of stardust. *Astrophys. J.* **780**, 95 (14pp).

Marhas K.K., Hoppe P. and Ott U. (2007) NanoSIMS studies of Ba isotopic compositions in single presolar silicon carbide grains from AGB stars and supernovae. Meteor. Planet. Sci. **42**, 1077-1101.

Marhas K.K., Amari S., Gyngard F., Zinner E. and Gallino R. (2008) Iron and nickel isotopic ratios in presolar SiC grains. *Astrophys. J.* **689**, 622-645.

Meyer B.S., Weaver T.A. and Woosley S.E. (1995) Isotope source table for a 25 $M_\odot$ supernova. *Meteoritics* **30**, 325-334.

Meyer B.S., Clayton D.D. and The L.-S. (2000) Molybdenum and zirconium isotopes from a supernova neutron burst. *Astrophys. J. Lett.* **540**, L49-L52.

Nicolussi G.K., Pellin M.J., Lewis R.S., Davis A.M., Clayton R.N. and Amari S. (1998) Zirconium and molybdenum in individual circumstellar graphite grains: New isotopic data on the nucleosynthesis of heavy elements. *Astrophys. J.* **504**, 492-499.

Nittler L.R. and Hoppe P. (2005) Are presolar silicon carbide grains from novae actually from supernovae? *Astrophys. J. Lett.* **631**, L89-L92.

Nomoto K., Kobayashi C. and Tominaga N. (2013) Nucleosynthesis in stars and the chemical enrichment of galaxies. *ARAA* **51**, 457-509.

Pellin M.J., Calaway W.F., Davis A.M., Lewis R.S., Amari S. and Clayton R.N. (2000) Toward complete isotopic analysis of individual presolar silicon carbide grains: C, N, Si, Sr, Zr, Mo, and Ba in single grains of type X. *LPI* **31**, 1917.

Pellin M.J., Savina M.R., Calaway W.F., Tripa C.E., Barzyk J.G., Davis A.M., Gyngard F., Amari S., Zinner E., Lewis R.S. and Clayton R.N. (2006) Heavy metal isotopic anomalies in supernovae presolar grains. *LPI* **37**, 2041.

Pignatari M., Wiescher M., Timmes F.X., de Boer R.J., Thielemann F.K., Fryer C., Heger A., Herwig F. and Hirschi R. (2013) Production of carbon-rich presolar grains from massive stars. *Astrophys. J.* **767**, L22 (26pp).

Pignatari M., Zinner E., Hoppe P., Jordan C.J., Gibson B.K., Trappitsch R., Herwig F., Fryer C., Hirschi R. and Timmes F.X. (2015) Carbon-rich presolar grains from massive stars: Subsolar $^{12}C/^{13}C$ and $^{14}N/^{15}N$ ratios and the mystery of ^{15}N. *Astrophys. J.* **808**, L43 (46pp).

Pignatari M., Herwig F., Hirschi R., Bennett M., Rockefeller G., Fryer C., Timmes F. X., Ritter C., Heger A., Jones S., Battino U., Dotter A., Trappitsch R., Diehl S., Frischknecht U., Hungerford A., Magkotsios G., Travaglio C., and Young P. (2016) NuGrid stellar data set. I. Stellar yields from H to Bi for stars with metallicities $Z = 0.02$ and $Z = 0.01$. *Astrophys. J. Supp. Ser.* **225**, 24 (54pp).

Pignatari M., Göbel K., Reifarth R., Travaglio C. (2016), The production of proton-rich isotopes beyond iron: The γ-process in stars, *International Journal of Modern Physics E*, **25**, 4, 1630003-232

Rauscher T., Heger A., Hoffman R.D. and Woosley S.E. (2002) Nucleosynthesis in massive stars with improved nuclear and stellar physics. *Astrophys. J.* **576**, 323-348.

Rauscher, T., Dauphas, N., Dillmann, I., Fröhlich, C., Fülöp, Zs, Gyürky, Gy (2013) *Reports on Progress in Physics*, **76**, 6, 066201

Savina M.R., Tripa C.E., Pellin M.J., Davis A.M., Clayton R.N., Lewis R.S., Amari S. (2003) Isotopic composition of molybdenum and barium in single presolar silicon carbide grains of type A+B. *LPI* **38**, 2231.

Savina M.R., Pellin M.J., Davis A.M., Lewis R.S., Amari S. (2007) p-process signature in a unique presolar silicon carbide grain. *LPI* **34**, 2079.

Stephan T., Trappitsch R., Davis A.M., Pellin M.J., Rost D., Savina M.R., Jadhav M., Kelly C.H., Gyngard F., Hoppe P., and Dauphas N. (2017) Strontium and barium isotopes in presolar silicon carbide grains measured with CHILI - two types of X-grains. *Geochim. Cosmochim. Acta* **this issue.**

Tagliente G., Lugaro M., Karakas A.I., Milazzo P.M.; nTOF Collaboration (2012) New ^{90,91,92,93,94,96}Zr neutron capture cross-sections. *PoS* **25**.

Thielemann F.-K., Arnould M., Hillebrandt W. (1979) Meteoritic anomalies and explosive neutron processing of helium-burning shells. *A&A* **74**, 175-185.

Thielemann, F.-K., Arcones, A., Käppeli, R., Liebendörfer, M., Rauscher, T., Winteler, C., Fröhlich, C., Dillmann, I., Fischer, T., Martinez-Pinedo, G., Langanke, K., Farouqi, K., Kratz, K.-L., Panov, I., Korneev, I. K. (2011) What are the astrophysical sites for the r-process and the production of heavy elements? *Progress in Particle and Nuclear Physics*, ***66***, Issue 2, 346-353

Woosley S.E., Heger A. and Weaver T.A. (2002) The evolution and explosion of massive stars, *Rev. Mod. Phys*. **74**, 1015-1071.

Zinner E., Jadhav M., Gyngard F., Nittler L.R. (2011) Bonanza, a huge presolar SiC Grain of type X, *LPI* **42**, 1070.

Zinner E. (2014) Presolar Grains. In *Meteorites and Cosmochemical Processes* (ed. A.M. Davis). Elsevier, Amsterdam, pp. 181-213.

FIGURE CAPTIONS

Figure 1. Isotopic abundance profiles after the SN explosion in the top of the O/C zone, the C/Si zone, and the He/C zone of the model 15d. We show the abundance profiles for ^{4}He, ^{12}C, ^{16}O and ^{28}Si, together with the stable Zr isotope ^{90,91,92,94,96}Zr abundances multiplied by 1000. All the unstable isotopes are assumed to have decayed completely to their stable daughter species. The numbers in the figure are used to identify the mass coordinates 2.95 $M_{\odot}$ (1), 3.15 $M_{\odot}$ (2), 3.50 $M_{\odot}$ (3) and 3.85 $M_{\odot}$ (4). Zone 4 is representative of the composition of the external He shell layers, carrying the pre-SN nucleosynthesis signature.

Figure 2. As in Fig. 1, but showing the abundances of directly produced ^{90}Zr and its radioactive precursors at about 2.5 seconds after the SN shock passage.

Figure 3. As in Fig. 1, but for the stable Mo isotopes ^{95,96,97,98,100}Mo.

Figure 4. As in Fig. 2, but showing the abundances of directly produced ^{100}Mo and its radioactive precursors.

Figure 5. (a) Production factors of the Zr isotopes, integrated over the different C-rich He-shell layers, and normalized to ^{94}Zr. For comparison, the profiles are shown for models 15d (black circles, see Fig. 1 and discussion in the previous section), 20d (blue triangles) and 25d (green squares). Data for two SiC X grains are shown by asterisk symbols and dashed lines. (b) As in Panel (a), but assuming a Sr:Zr fractionation of 1:10.

Figure 6. (a) As in Fig. 5a, but with integrating over the different C-rich He-shell layers weighting by mass and "efficient" ^{12}C (see text for explanation). The solar-normalized ^{12}C/^{13}C, ^{29}Si/^{28}Si and ^{30}Si/^{28}Si ratios for this mixture are 5051, 1.31 and 2.09 (15d), 42918, 1.92 and 3.51 (20d) and 0.72, 7.62 and 3.63 (25d). (b) As in panel (a), but with integrating over the different C-rich He-shell layers weighting by mass, "efficient" ^{12}C and Si abundance. The solar-normalized ^{12}C/^{13}C, ^{29}Si/^{28}Si and ^{30}Si/^{28}Si ratios for this mixture are 99010, 0.31 and 0.85 (15d), 990099, 1.36 and 2.86 (20d) and 16.67, 8.03 and 3.92 (25d).

Figure 7. As in Fig. 5, but for Mo isotopes, normalized to ^{98}Mo.

Figure 8. For model 15d, the integrated Mo abundance distribution shown in Figure 7 is compared with the local abundances in zones 1, 2, 3 and 4 only (see Figure 3).

Figure 1

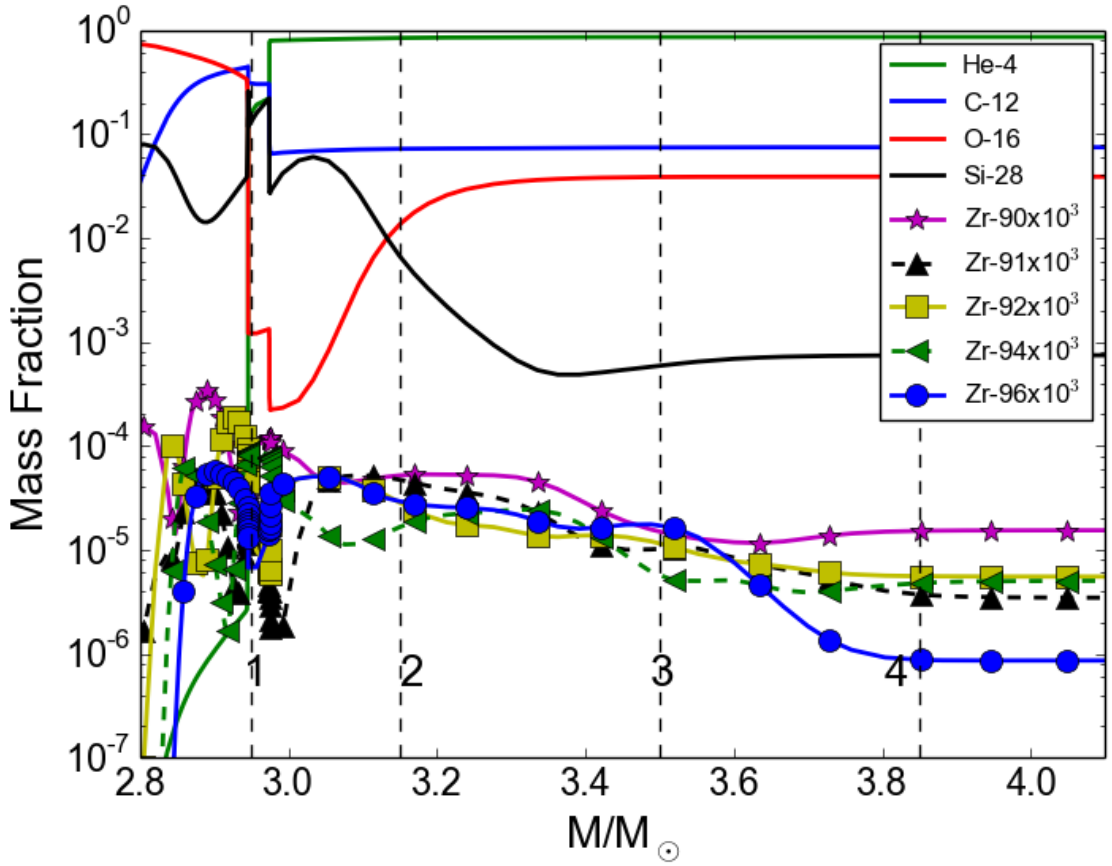

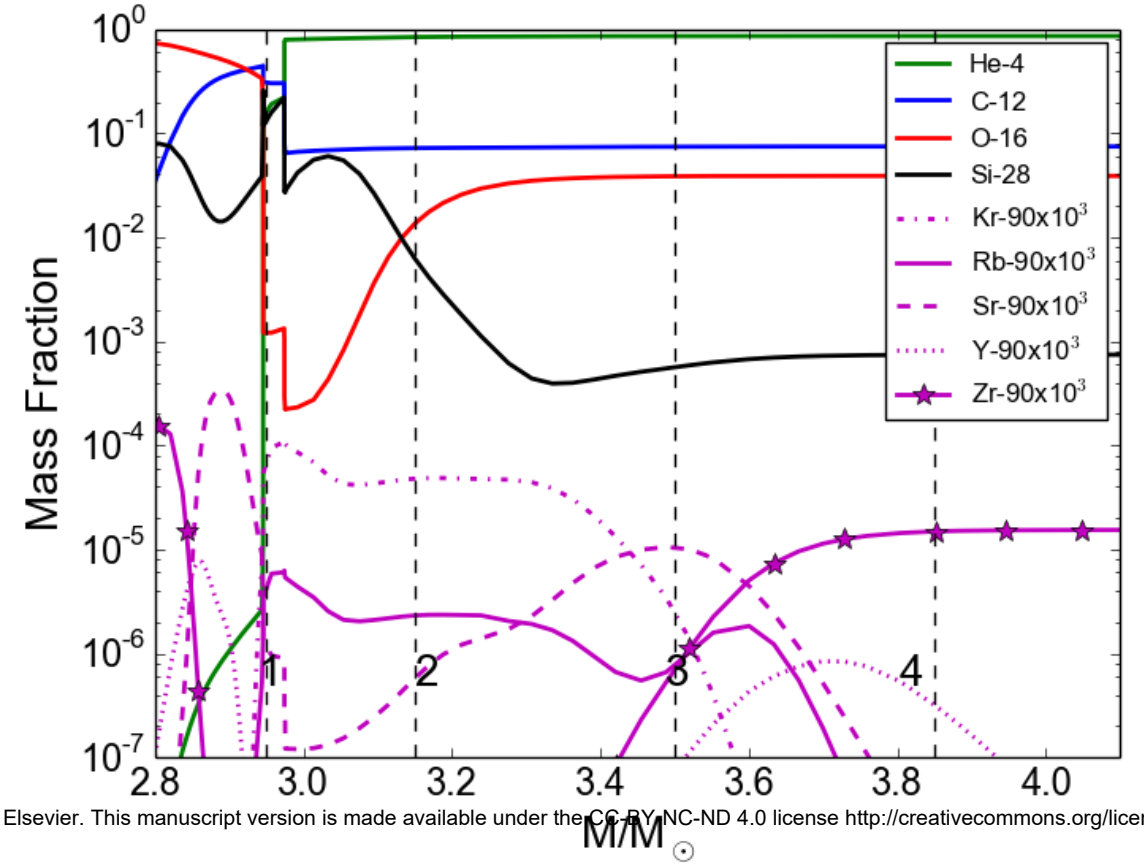

Figure 2

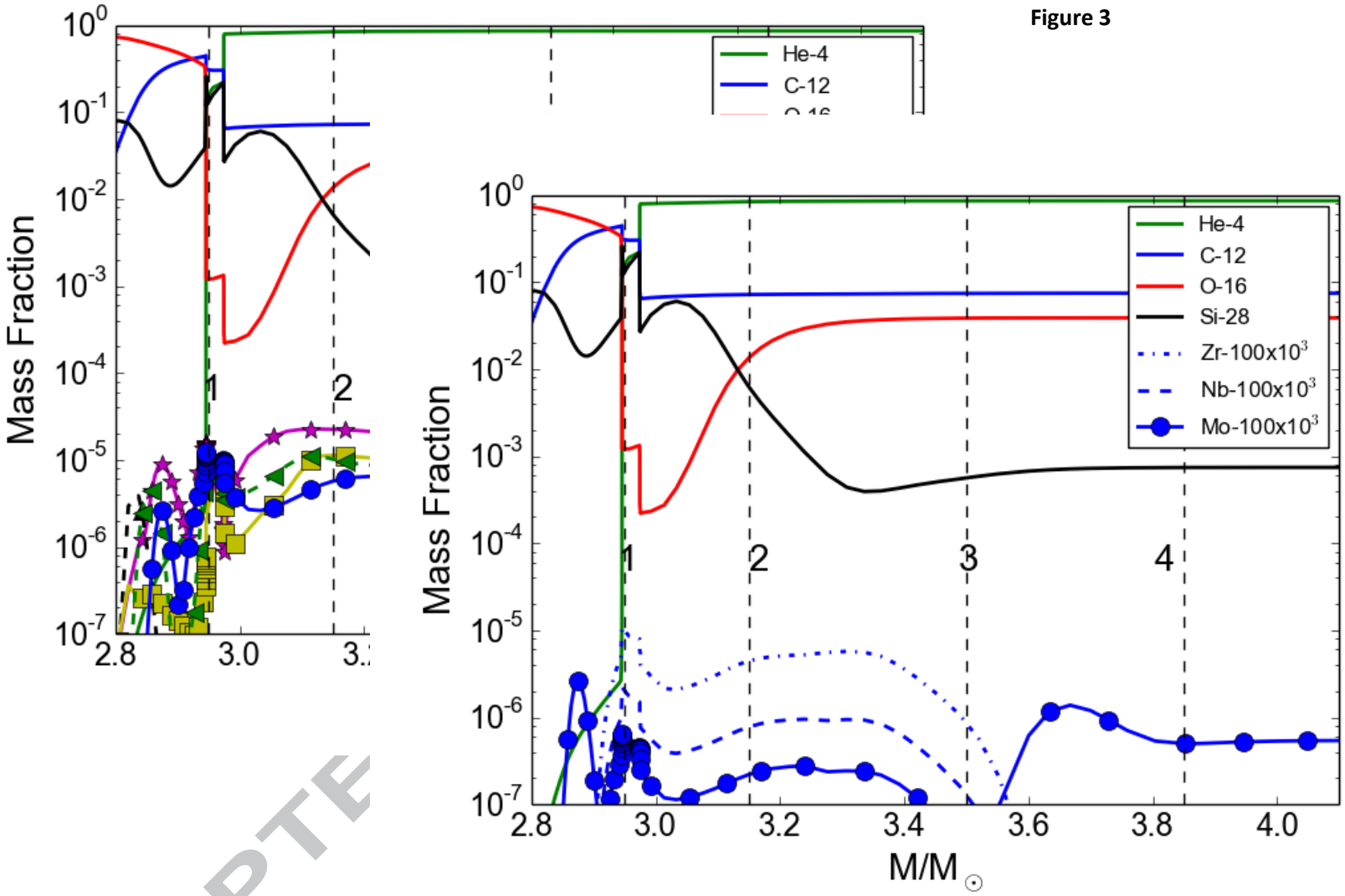

Figure 3

Figure 4

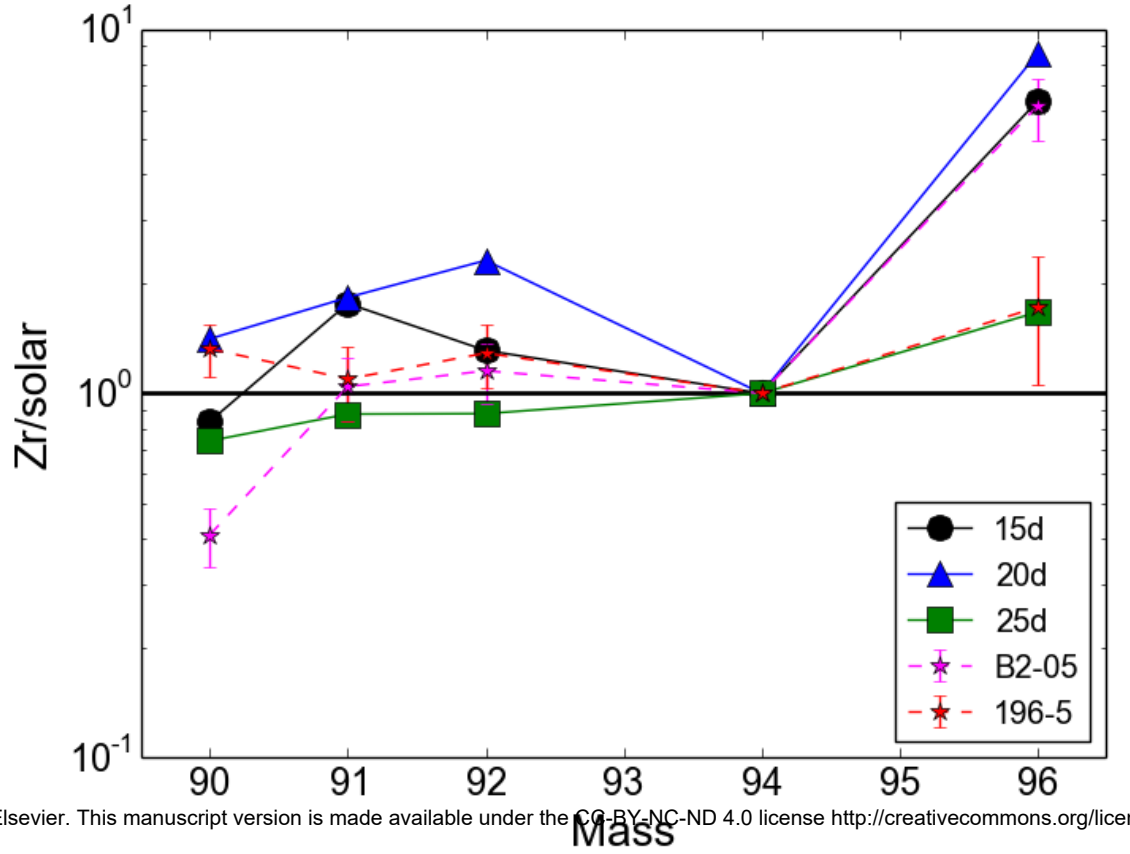

Figure 5a

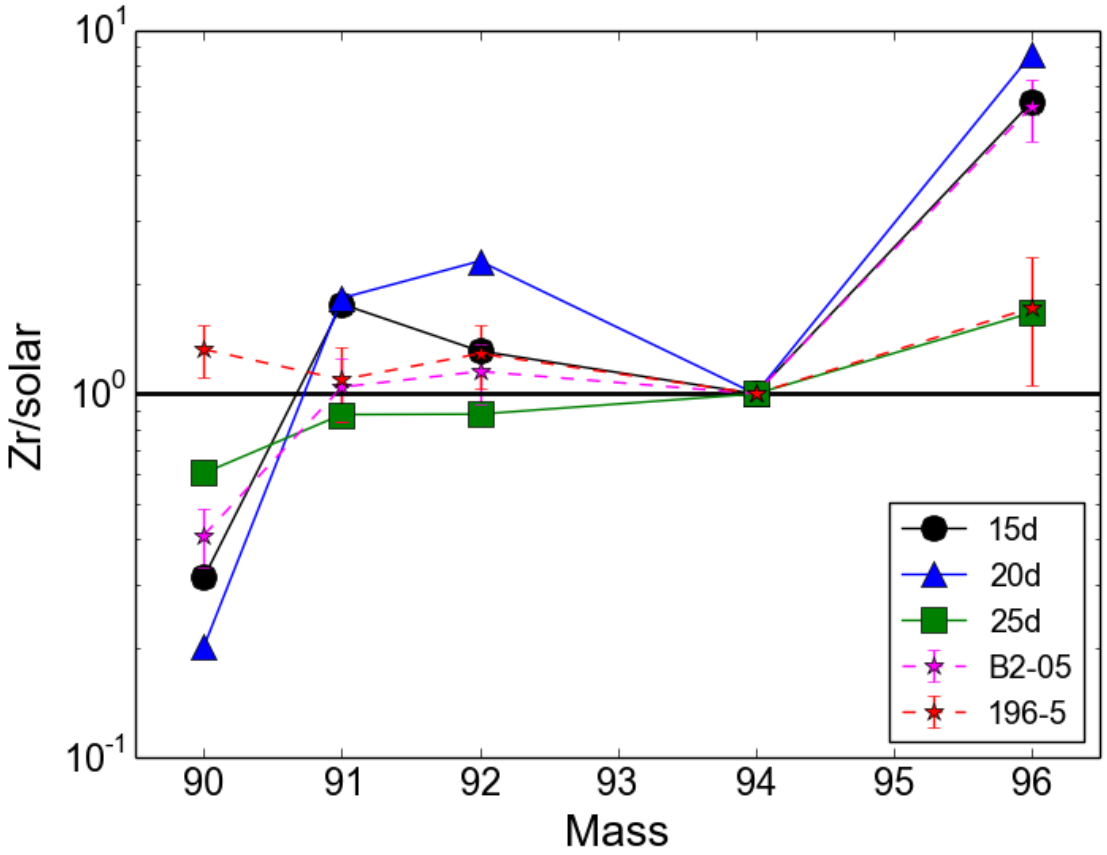

Figure 5b

Figure 6a

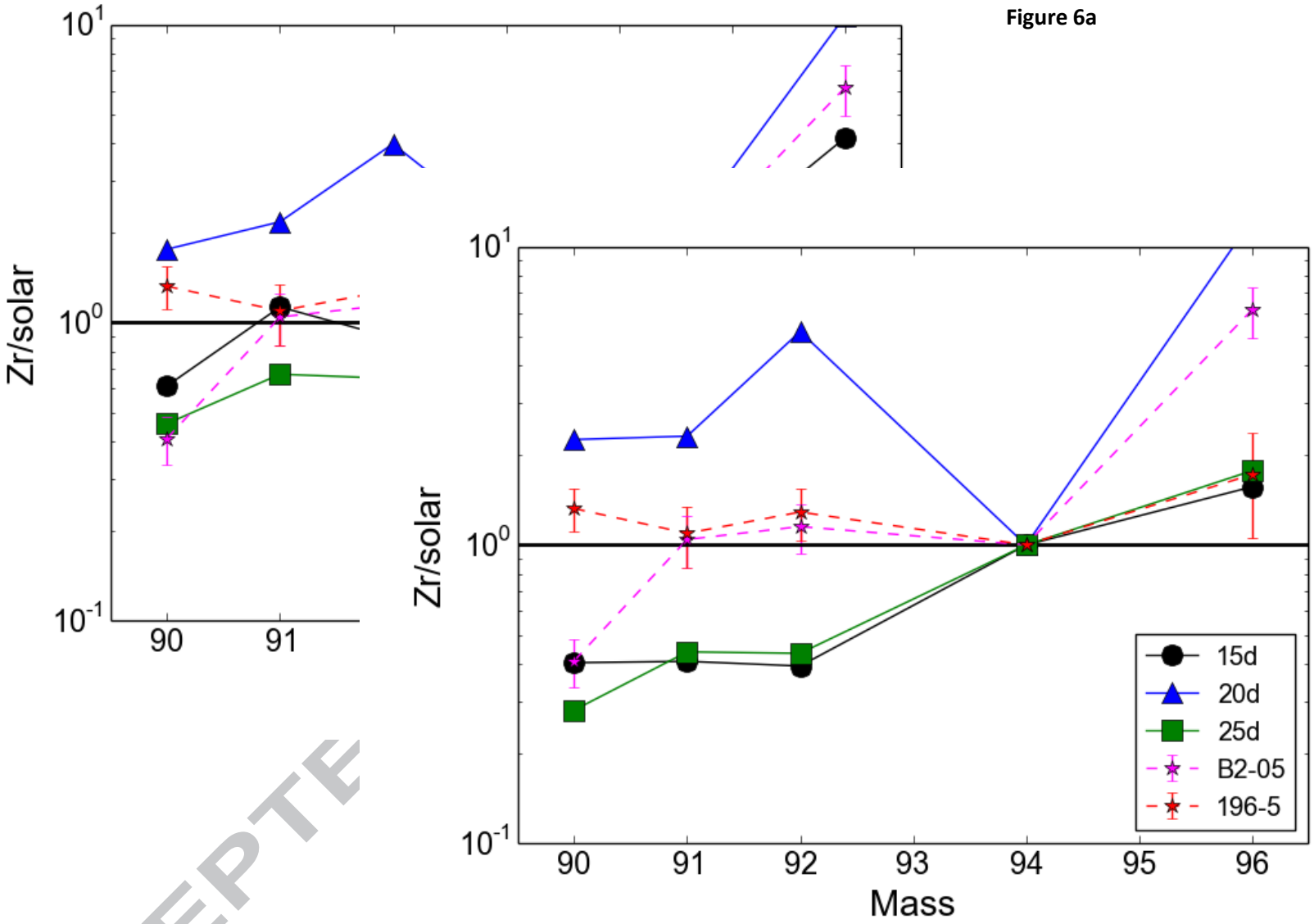

Figure 6b

Figure 7

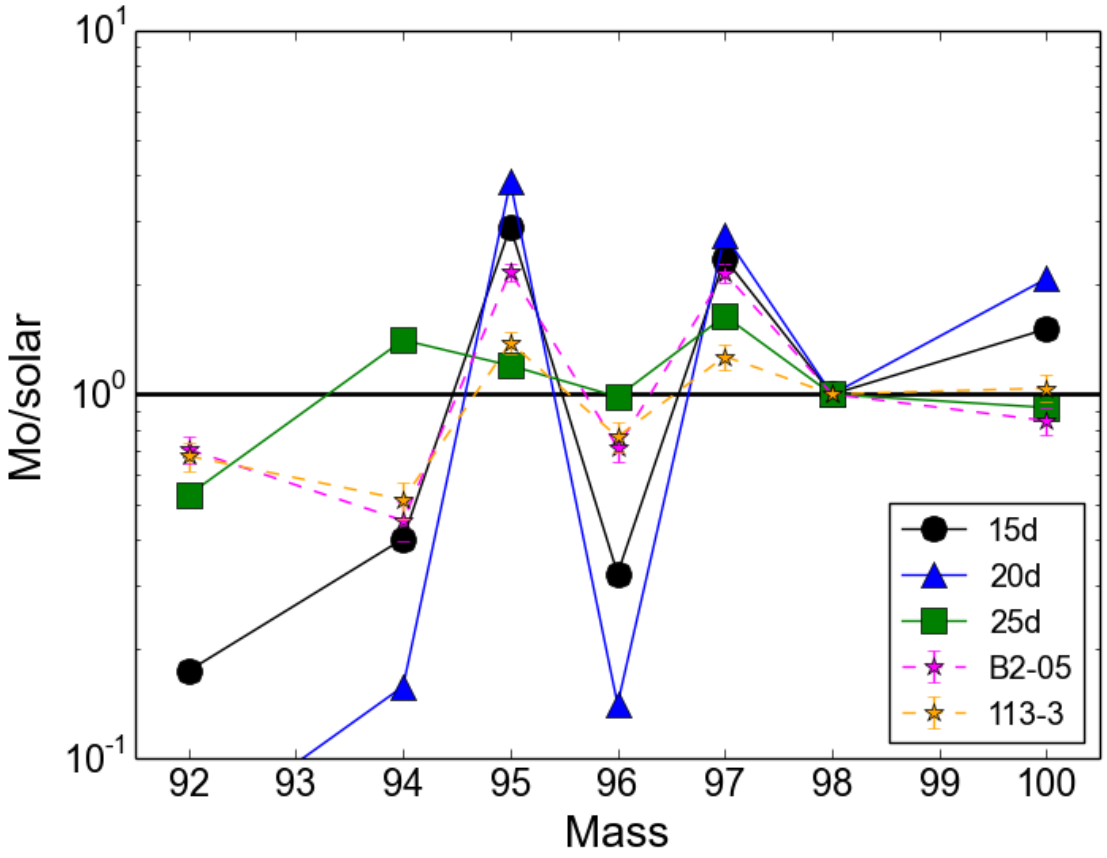

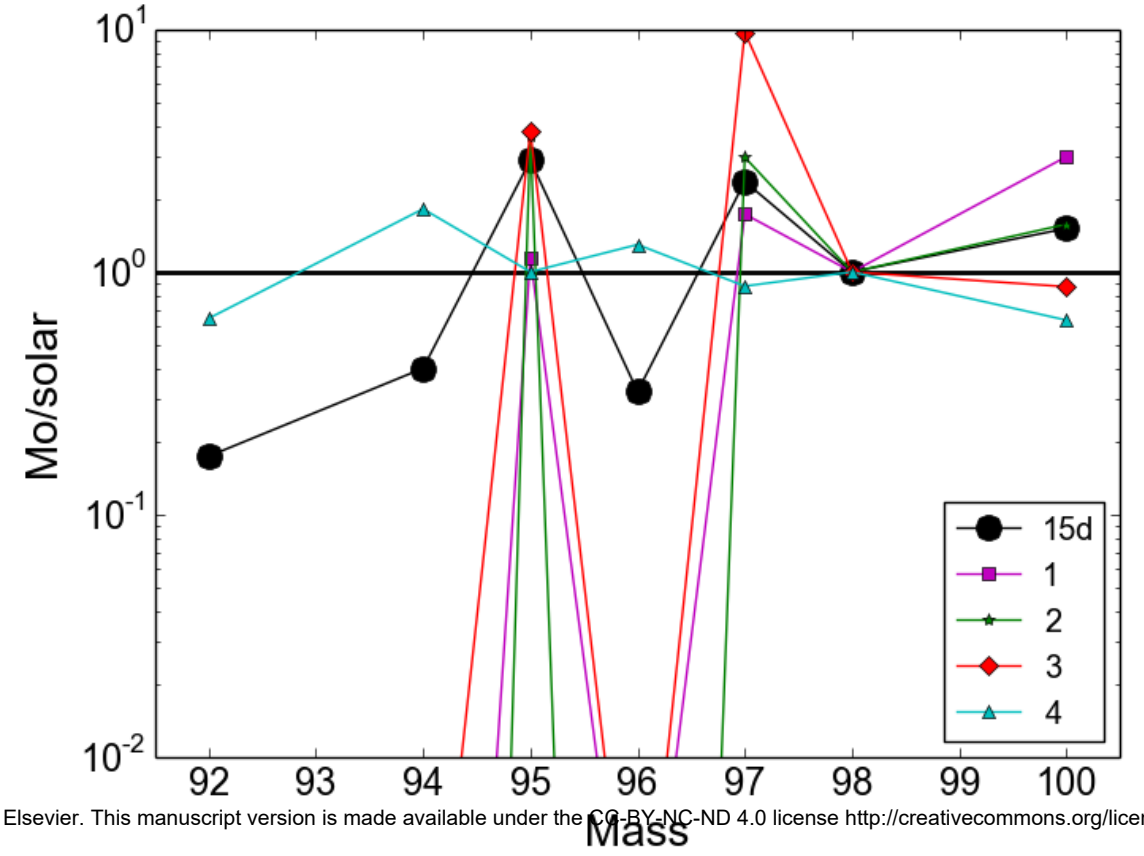

Figure 8

Table 1. Average isotopic compositions of models 15d, 20d and 25d in the C-rich He shell, for Zr and Mo. The Zr production factors are normalized to ^{94}Zr, while for Mo the reference isotope is ^{98}Mo. The average is weighted by mass.

Model	^{90}Zr	^{91}Zr	^{92}Zr	^{94}Zr	^{96}Zr	^{92}Mo	^{94}Mo	^{95}Mo	^{96}Mo	^{97}Mo	^{98}Mo	^{100}Mo
15d[1]	0.838 (0.313)[2]	1.765	1.311	1.0	6.329	0.174	0.401	2.886	0.322	2.359	1.0	1.512
20d[1]	1.412 (0.202)[2]	1.834	2.318	1.0	8.560	0.060	0.157	3.829	0.141	2.737	1.0	2.078
25d[1]	0.741 (0.606)[2]	0.877	0.880	1.0	1.670	0.529	1.409	1.200	0.985	1.641	1.0	0.920

[1] The ^{12}C/^{13}C, ^{29}Si/^{28}Si and ^{30}Si/^{28}Si ratios normalized to solar for the mixture are 1449, 3.09 and 4.02 (15d), 16234, 2.81 and 4.34 (20d) and 0.31, 5.81 and 3.04 (25d). See the text and Figure 5 for discussion.

[2]The ^{90}Zr production factor normalized to ^{94}Zr, assuming a Zr/Sr fractionation of 10. See text for details.

Table 2. Average isotopic compositions of models 15d, 20d and 25d in the C-rich He shell, for Zr and Mo. The Zr production factors are normalized to ^{94}Zr, while for Mo the reference isotope is ^{98}Mo. The average is weighted by mass and "efficient" ^{12}C ($\Delta(^{12}C) = X(^{12}C)-X(^{16}O)$).

Model	^{90}Zr	^{91}Zr	^{92}Zr	^{94}Zr	^{96}Zr	^{92}Mo	^{94}Mo	^{95}Mo	^{96}Mo	^{97}Mo	^{98}Mo	^{100}Mo
15d[1]	0.613	1.128	0.888	1.0	4.166	0.109	0.255	2.765	0.205	2.074	1.0	1.907
20d[1]	1.764	2.180	3.982	1.0	10.663	0.038	0.100	3.785	0.095	2.315	1.0	2.178
25d[1]	0.458	0.671	0.650	1.0	2.070	0.267	0.719	1.818	0.509	2.815	1.0	1.425

[1] The $^{12}C/^{13}C$, $^{29}Si/^{28}Si$ and $^{30}Si/^{28}Si$ ratios normalized to solar for the mixture are 5051, 1.31 and 2.09 (15d), 42918, 1.92 and 3.51 (20d) and 0.72, 7.62 and 3.63 (25d). See the text and Figure 6 for discussion.

Table 3. Average isotopic compositions of models 15d, 20d and 25d in the C-rich He shell, for Zr and Mo. The Zr production factors are normalized to ^{94}Zr, while for Mo the reference isotope is ^{98}Mo. The average is weighted by mass, "efficient" ^{12}C ($\Delta(^{12}C) = X(^{12}C)-X(^{16}O)$) and the Si abundance.

Model	^{90}Zr	^{91}Zr	^{92}Zr	^{94}Zr	^{96}Zr	^{92}Mo	^{94}Mo	^{95}Mo	
15d[1]	0.403	0.407	0.393	1.0	1.567	0.001	0.004	2.045	0
20d[1]	2.257	2.318	5.197	1.0	12.308	0.001	0.002	3.852	0
25d[1]	0.279	0.438	0.433	1.0	1.774	0.009	0.025	1.772	0

[1] The ^{12}C/^{13}C, ^{29}Si/^{28}Si and ^{30}Si/^{28}Si ratios normalized to solar for the mixture are 99010, 0.31 and 0.85 (15d), 990099, 1.36 and 2.86 (20d) and 16.67, 8.03 and 3.92 (25d). See the text and Figure 6 for discussion.